Fast age-hardening response of Al–Mg–Si–Cu–Zn–Fe–Mn alloy via coupling control of quenching rate and pre-aging

Yuan, Bo; Li, Gaojie; Guo, Mingxing; Zhuang, Linzhong

DOI
10.1016/j.jmrt.2021.07.067

Publication date
2021

Document Version
Final published version

Published in
Journal of Materials Research and Technology

Citation (APA)
Yuan, B., Li, G., Guo, M., & Zhuang, L. (2021). Fast age-hardening response of Al–Mg–Si–Cu–Zn–Fe–Mn alloy via coupling control of quenching rate and pre-aging. *Journal of Materials Research and Technology*, *14*, 1518-1531. https://doi.org/10.1016/j.jmrt.2021.07.067

JOURNAL OF MATERIALS RESEARCH AND TECHNOLOGY 2021;14:1518–1531

Available online at www.sciencedirect.com

jmr&t Journal of Materials Research and Technology

journal homepage: www.elsevier.com/locate/jmrt

Original Article

Fast age-hardening response of Al–Mg–Si–Cu–Zn–Fe–Mn alloy via coupling control of quenching rate and pre-aging

Bo Yuan [a], *Gaojie Li* [c], *Mingxing Guo* [a,b,*], *Linzhong Zhuang* [a,b,**]

[a] *State Key Laboratory for Advanced Metals and Materials, University of Science and Technology Beijing, Beijing, 100083, China*
[b] *Beijing Laboratory of Metallic Materials and Processing for Modern Transportation, University of Science and Technology Beijing, Beijing, 10083, China*
[c] *Department of Materials Science and Engineering, Delft University of Technology, 2628 CD Delft, the Netherlands*

ARTICLE INFO

Article history:
Received 31 May 2021
Accepted 13 July 2021
Available online 17 July 2021

Keywords:
Al–Mg–Si–Cu–Zn–Fe–Mn alloy
Coupling control
Paint baking
Precipitation
Yield strength

ABSTRACT

The coupling control of quenching rate and pre-aging and its positive effect on the age-hardening response of Al–Mg–Si–Cu–Zn–Fe–Mn alloy was systematically investigated. The larger and more stable solute clusters can be formed in alloy with fast age-hardening response by using the lower quenching rate (5.3 °C/min) and an appropriate pre-aging, in which the deterioration of natural aging also can be obviously suppressed. Additionally, the highest bake hardening increment of the alloy can reach 145.2 MPa, which is much higher than those of traditional Al–Mg–Si–(Cu) alloys (such as, 6016 and 6111 alloys). Based on the detailed precipitation behavior characterization of alloys with different quenching rates and the same pre-aging, the quenching rate change can result in the significant differences in the size, number density of precipitates in the both paint baking and peak aging states, but the type of precipitates basically keeps the same, i.e., Mg–Si precipitates, and no Mg–Zn precipitates can be observed. Finally, the related mechanisms of coupling control of quenching rate and pre-aging were also discussed in this paper. The developed coupling control method shows great potential and could significantly increase applications of Al–Mg–Si–Cu–Zn–Fe–Mn alloys with a fast age-hardening response.

---

[*] Corresponding author.
[**] Corresponding author.

E-mail addresses: mingxingguo@skl.ustb.edu.cn (M. Guo), linzhongzhuang@yahoo.com (L. Zhuang).

https://doi.org/10.1016/j.jmrt.2021.07.067

1. Introduction

It has been found that Al–Mg–Si alloys normally possess an excellent formability, corrosion resistance, age-hardening response and bendability [1–6]. Thus, they have been believed an important material for weight reduction of automobiles. However, their mechanical properties, such as, strengths and formability, are still much lower than those of steels for automotive applications. Accordingly, in order to meet the demanding requirements of automotive applications, these properties still need to be further enhanced [7], especially for the bake hardening response. The paint baking process is similar as the heat treatment at 170–185 °C for 20–30 min [6], which normally stays in the under-aging state, and corresponding to lower strengths. Although the age-hardening response of Al–Mg–Si–Cu alloys have been believed much better than those of other series Al alloys, up to date, the bake hardening increment of Al–Mg–Si series alloys only increases from 30—40 MPa to 80–120 MPa by optimizing composition and pre-aging [4,5,8–10]. With the development of car industry, it is greatly necessary to find a good way to further improve the age hardening response of Al–Mg–Si alloys.

There are many published reports showing an adverse effect of natural aging on high temperature age hardening behaviors of the Al–Mg–Si–Cu alloys [8–13]. In order to avoid the adverse effect, many works on composition optimization and processing route controlling have been done in the past years. For examples, the Mg/Si ratio of solute clusters formed during natural aging is vastly dependent on the composition or Mg/Si ratio of alloys, and Mg–Mg, Si–Si or Mg–Si clusters with a lower or a wide range of Mg/Si ratio are quite difficult to directly transform into stable β″ phase during the followed bake hardening treatment, which directly results in the lower bake hardening increment for natural aged Al–Mg–Si alloys [9,11]. Additionally, it has been found that the addition of Cu or Zn is an effective way to avoid the adverse effect of natural aging on bake hardening response of Al–Mg–Si alloys [8,10,12,13]. The addition of Cu mainly improves the formation of stable Mg–Si solute clusters [12,13], while Zn addition could help the formation of stable Mg–Si–Cu–Zn complex solute clusters with a high Mg/Si ratio, finally, all of these stable clusters are easy to be transformed into the Mg–Si precipitates (such as β″ [10,13], or Zn-containing β″precipitates [8,14–16]) during bake hardening or artificial aging treatment. Apart from these improvements, it has been also reported that the addition of trace amount of Sn or In could suppress natural aging up to two weeks, which was believed as result of the strong ability of trapping vacancies by Sn or In atoms [17,18]. However, with the change of alloy composition, such as in Zn-free or Zn-added Al–Mg–Si–Cu alloys, the positive effect of micro-alloying elements on paint bake hardening response would be also changed significantly, and even completely disappears in the Zn-containing Al–Mg–Si–Cu alloys.

Beside the design and optimization of alloy composition, an appropriate pre-aging treatment has proved to be effective method to avoid the adverse effect of natural aging and improve the bake hardening increment of Al–Mg–Si–Cu alloys [8,10,19–24]. Certainly, with the change of alloy composition, both the appropriate temperature and time of pre-aging would change accordingly, which are very crucial to better control the size, morphology, composition and distribution of solute clusters formed in the pre-aged alloys [8,10,19–24]. There is a general agreement that a pre-aging treatment in the temperature range of 70–130 °C after quenching provides an effective way to control the distribution of solute clusters and increase the number density of Mg–Si or Zn-containing Mg–Si precipitates during subsequent bake hardening treatments [8,10,19–24]. It has been postulated that treatment in this temperature range facilitates the formation of Mg–Si co-clusters with both a uniform Mg/Si ratio and an appropriate size, which can either transform into β″ phase or serve as nuclei for precipitation of the β″ phase [22–24]. Accordingly, an appropriate pre-aging treatment is greatly important to enhance the bake hardening increments of Al–Mg–Si–Cu or Al–Mg–Si–Cu–Zn alloys. However, it is also very important to well control the solution treatment, quenching method and rate before a pre-aging treatment in Al–Mg–Si–Cu–(Zn) alloys, because they directly affect the nucleation and growth of solute clusters during the pre-aging treatment. Thus, they should be also carefully considered during the design and optimization of pre-aging treatment.

Up to date, it has been found that the number density of vacancies in AA6016 alloys could be markedly reduced by decreasing the quenching rate after solution treatment [25–29], and the precipitation evolution, corrosion behavior and bendability are all correlated with the quenching rate used in the Al–Mg–Si–Cu alloys. For example, crack propagation during bending test of AA6016 alloy is decreased after rapid quenching, which mainly results from the formation of Mg_2Si instead of Si grain boundary precipitates during quenching process [28]. The interrupted quenching in the temperature range 150–250 °C for periods of 15–1080 s gives a great influence on artificial aging of AA6016 Al alloy after long-term natural pre-aging [29]. It has been found that the age hardening kinetics could be enhanced in the interrupted quenched alloy at low temperatures but reduced at high temperatures, and the formed vacancies were found to be of particular importance for the nucleation of precipitates occurring during the interrupted quenching process. Additionally, quenching rate also gives a great influence on the microstructure and properties of Al–Zn–Mg–Cu alloys [30,31]. Thus, it could be expected that both the quenching method and quenching rate will show a notable impact on age hardening response of Al–Mg–Si–Cu alloys with 3.0 wt.% Zn. To better design a suitable pre-aging treatment, it is necessary to systematically study the synergistic influence of quenching rates and pre-aging on the age-hardening behaviors of Al–Mg–Si–Cu–Zn–Fe–Mn alloys. The purpose of this study is to find a remarkable way to improve the bake hardening increment of Zn-containing Al–Mg–Si–Cu alloys based on the comprehensive understanding the related coupling control mechanisms of quenching rate and pre-aging.

2. Experimental

The chemical composition of experimental alloy is Al–0.8Mg–1.2Si–0.5Cu–3Zn–0.5Fe–0.3Mn (wt.%). The alloy was prepared with high-purity aluminum (99.99 wt.%), industrial Mg, industrial pure Zn, Al–20Si, Al–50Cu, Al–10Mn, Al–20Fe (wt.%), and a grain refining agent Al–5Ti–1B (wt.%). The raw materials were melted in a graphite crucible in an electrical resistance furnace (SG2-12-10)and then cast into an ingot with a size of 220 mm (length) × 120 mm (width) × 100 mm (thickness) in steel mold. The ingot was homogenized at 485 °C for 3 h + 555 °C for 30 h. After homogenization treatment, 5 mm was removed from each side to ensure consistent quality of the ingot. Subsequently, the ingots were hot-rolled at an initial temperature of 555 °C and a relatively low exit temperature below 300 °C from 90 mm to 4 mm, then the hot rolled alloy sheets were annealed at 400 °C for 1 h, then cold rolled to the final sheets with a thickness of 1 mm. The final cold rolled alloy sheets were solution treated at 555 °C for 2 min followed by different quenching rates as shown in Fig. 1. Varied rates were obtained by quenching to different mediums: (Quenching rate I) to 20 °C water; (Quenching rate II) to 50 °C water; (Quenching rate III) to 90 °C water; (Quenching rate IV) to 20 °C oil; subsequently the samples were directly pre-aged at 80 °C for 2 h (pre-aging) followed by artificial aging at 185 °C, or pre-aged at 80 °C for 2 h (pre-aging) + natural aging for 14 days (T4P) + artificial aging at 185 °C, to compare their age hardening responses.

The Vickers hardness (HV) measurement were carried out on a 401 type MVD Vickers hardness (HV) instrument with a load of 200 g for 10 s, each sample was measured 5 times, and an average value was obtained based on them. Tensile tests were performed on a MTS810 testing machine with a tensile speed of 3 mm/min, the tensile samples were cut along the rolling direction, three samples were tested and then the average strengths and elongations were obtained based on the all values. Precipitation kinetics of the alloys in the different aging conditions was also characterized by differential scanning calorimeter (DSC). DSC tests were conducted in a Polyma DSC 214 instrument with an argon atmosphere from room temperature to 375 °C with a heating rate of 10 °C/min. The exact heat flow of samples with a size of Φ3 × 1 mm was finally obtained by subtracting that of pure aluminum with a similar shape and mass.

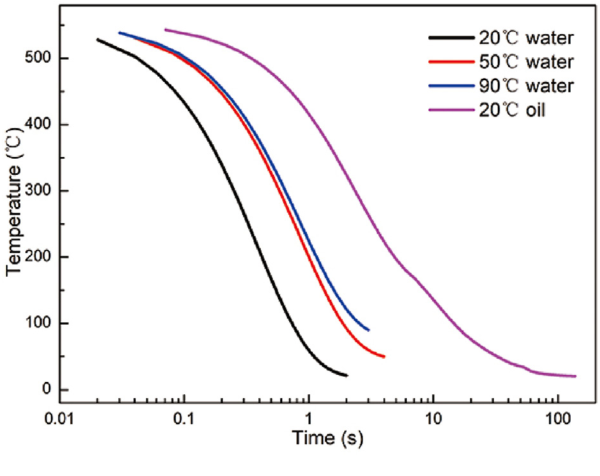

Fig. 1 – The quenching rates of solution treated alloy sheets.

The crystal structure, morphology, distribution and orientation of the precipitates in aged alloys were characterized on a TecnaiG2 F30 high resolution transmission electron microscopy (HRTEM), the coarse precipitates were analyzed by selected-area diffraction (SAD); the operating voltage used was 300 kV, along [001] direction of Al matrix. Thin foils for HRTEM studies were first mechanically ground to a thickness of around 100 μm, and then twin-jet polished in a solution of 30 vol.% nitric acid and 70 vol.% methanol at a temperature of −25 °C ~ −10 °C, and voltage of 20–30 V.

3. Results

3.1. *DSC analysis*

The pre-aged alloys with different quenching rates after solution treatment were firstly analyzed by differential scanning calorimeter(DSC) with a heating rate of 10 °C/min as shown in Fig. 2(a). The general trend of curves is similar, including three exothermic peaks *a*, *c*, *d* and one endothermic peak *b* in the DSC curves of the pre-aged alloys. However, the areas and starting temperatures of peaks change a lot with the change of quenching rates, indicating different precipitation behaviors, as shown in Fig. 2(a). Additionally, if the natural aging process of 14 days added after pre-aging, the treated alloys show different precipitation behaviors as changed DSC curves shown in Fig. 2(b). Although the three exothermic peaks *a*, *c*, *d* and one endothermic peak *b* still can be observed in the DSC curves, yet, a great change, especially for the peaks *a* and *b*, can be seen in the curves. This change indicates that natural aging also give a great influence on the precipitation of non-isothermal heat treatment (i.e., DSC heating process).

For the alloys without natural aging process, it has been found that with the increase of quenching rate, the area of peak *a* is also increased, indicating more solute clusters have been formed during DSC heating process, the nucleation of the new phase conforms to the Kolmogorov crystallization theory [32]. This mainly results from the fact that the higher vacancy concentration could be remained in quenched alloy matrix with a higher quenching rate, which could further help the formation of much more solute clusters during the heating process. It has been calculated that the solute–vacancy binding energies in Al matrix of Mg-, Si-, and Zn- are −0.01 ± 0.04, 0.03 and 0.02 ev, respectively [33]. The diffusion coefficient *D* of Mg, Si, and Zn in Al matrix can be calculated as 7.4×10^{-25}, 5.4×10^{-23}, and 7.8×10^{-23} at 80 °C [34,35], respectively, as shown in Table 1. Thus, Mg–Si, Si-rich, Mg–Zn and Mg–Si–Zn solute clusters could be formed during the pre-aging treatment [8,36–39]. Additionally, the peak *a* in the alloys treated by the pre-aging and natural aging of 14 days almost disappear (as shown in Fig. 2(b)), which indicates that the remained vacancies should be further combined with some solute atoms to reduce the possibility of forming solute clusters during the low temperature DSC heating process.

Additionally, peak *b* is corresponding to the GP zone dissolution (as shown in Fig. 2(a)), and the area is reduced with the increase of quenching rate. For the rapid quenched alloys, large defects (vacancy and dislocation) can be produced, they can help the formation and growth of solute clusters during

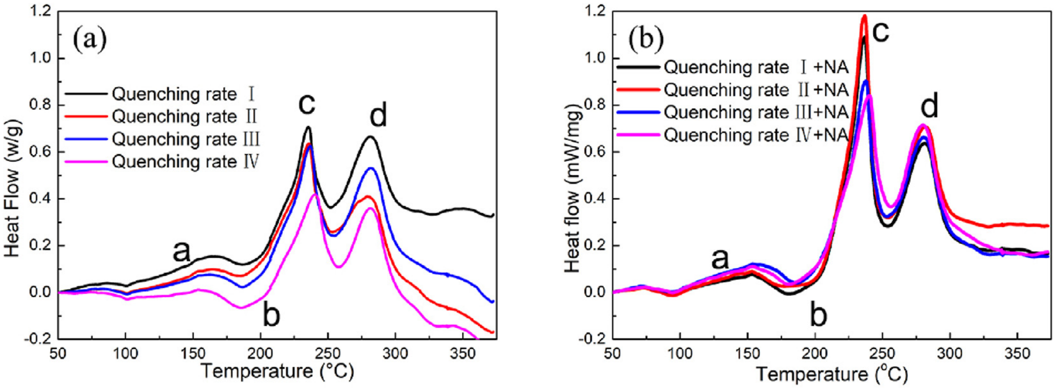

Fig. 2 – The DSC curve of alloys treated with different quenching rates, (a) pre-aging state, (b) pre-aging + natural aging for 14 days.

Table 1 – Diffusion coefficient of element in Al matrix at different temperature and related function.

	D ($m^2\ s^{-1}$)	353 K (80 °C)	458 K (185 °C)	523 K (250 °C)
Mg [34]	4.4×10^{-4} exp(−140,300/RT)	7.4×10^{-25}	4.4×10^{-20}	4.2×10^{-18}
Si [35]	1.4×10^{-5} exp(−117,600/RT)	5.4×10^{-23}	5.3×10^{-19}	2.5×10^{-17}
Zn [35]	1.2×10^{-5} exp(−116,100/RT)	7.8×10^{-23}	6.8×10^{-19}	3.0×10^{-17}

pre-aging treatment and DSC heating process, which directly result in the size of clusters above the critical dissolution size. And finally, they are difficult to be dissolved during this temperature range. However, for the alloys treated by pre-aging and natural aging of 14 days, the area of peak *b* decreases slightly with the reduction of quenched rate (as shown in Fig. 2(b)). This difference mainly results from the consumption of vacancy during natural aging, and the remained vacancy gives a poor effect on the growth of formed solute clusters and the formation of other new solute clusters during DSC heating process.

With the increase of heating temperature, peak *c* with a peak temperature of around 230 °C can be observed in the DSC curves (as shown in Fig. 2). This peak is normally corresponding to the formation of β″ phase [40]. With the increase of quenching rate, the starting temperature of peak *c* is decreased, corresponding to the increased precipitation kinetics. However, if the pre-aged alloys are further natural aged for 14 days, this difference basically cannot be clearly observed (as shown in Fig. 2(b)). This change should be caused by the interaction between remained vacancies in the alloys and solute atoms, and the formation of fine solute clusters during natural aging. As a result, the consumption of remained vacancies cannot further positively affect the formation of β″ phase, only the stable Mg–Si–Cu–Zn solute clusters can be transformed into β″ phase. Therefore, the starting temperature of peak *c* is basically the same, the peak area changes with the changed number density of solute clusters that formed during the pre-aging treatment. Finally, the peak *d* normally corresponds to the precipitation of β′ or Q′ phases [40], here it is not necessary to discuss this peak in depth.

The precipitation kinetics of β″ phase can be analyzed by the modified Avrami–Johnson–Mehlmodel [30,31,33] as follows:

$$Y = 1 - \exp\left[-(kt)^n\right] \tag{1}$$

$$K = k_0 \exp\left(\frac{Q}{RT}\right) \tag{2}$$

where Y is the volume fraction, t represent time, $n = 2$ for the β″ formation model [41], k_0 is constant, Q is the activation energy, R = 8.31 J/(mol K) is the gas constant, T is the thermodynamic temperature. The final equation can be obtained as follows:

$$\ln\left[\left(\frac{dY}{dT}\right)\frac{\varphi}{f(Y)}\right] = \ln k_0 - \left(\frac{Q}{R}\right)\left(\frac{1}{T}\right) \tag{3}$$

where *f(Y)* is implicit function about Y, from the linear regression of left-hand side of equation (3) versus 1/*T* as shown in Fig. 3(b) and (d), Q value can be determined by experimentally, and then the precipitation kinetics equations can be established as shown in Table 2.

According to the results shown in Table 2, the activation energy of β″ phase formation in alloys changed obviously with different quenching rate. As the quenching rate increases, the activation energy of β″ precipitation in pre-aged alloys also increases. The activation energies of alloys with quenching rate I, II and III are 34.8 kJ/mol, 40.2 kJ/mol, and 42.2 kJ/mol, respectively. With the change of quenching medium from water to oil, and the activation energy of quenching rate IV alloy is the maximum, i.e., 53.2 kJ/mol. Interesting, for the alloys treated by pre-aging + natural aging of 14 days, the change trend of the activation energy of β ″ precipitation is completely different from that of pre-aged alloys. The activation energy of β ″ precipitation in the alloys is increased with the introduction of natural aging, the activation energies of alloys with quenching rate I, II and III are 70.2 kJ/mol, 69.4 kJ/mol and 62.4 kJ/mol, respectively. However, the natural aging gives a poor effect on the activation energy of β″

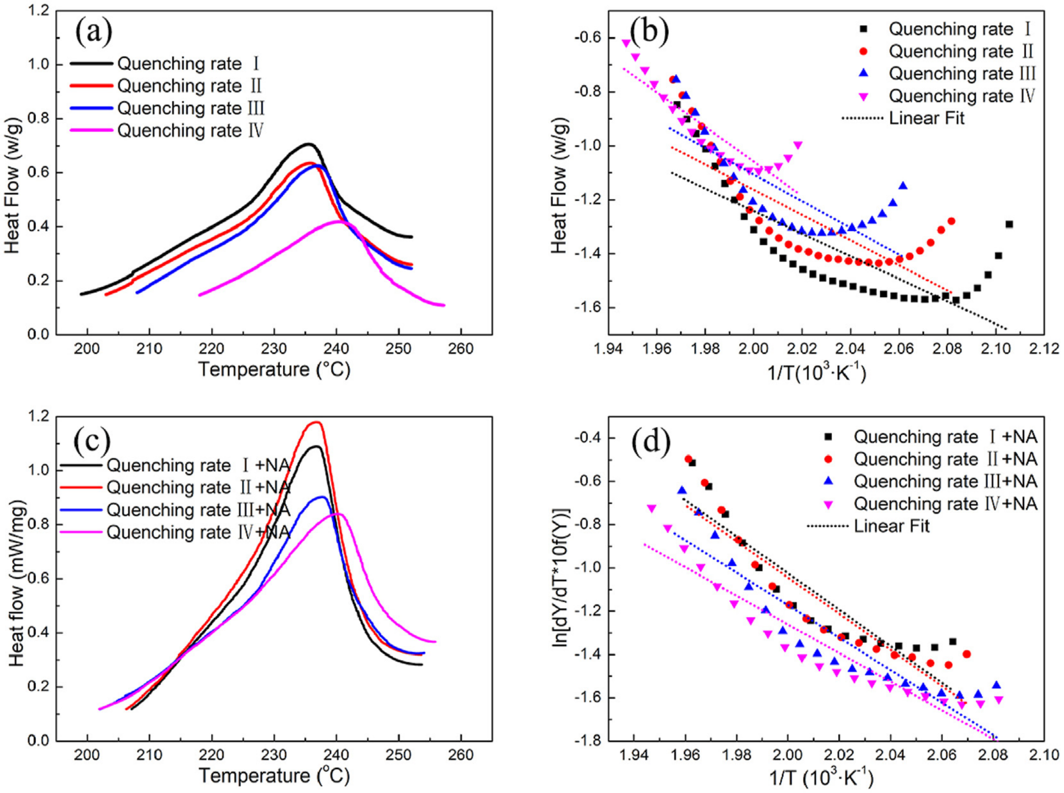

Fig. 3 – The β″ phase formation zones of four different kinds of quenching rate alloy in pre-aging or pre-aging + 14 day natural aging state (a), (c), corresponding activation energy diagram (b), (d).

Table 2 – The activation energy and precipitation kinetics of β″ phases formed in the alloys.

Pathways	Q ($kJ\cdot mol^{-1}$)	k_0 (min^{-1})	Precipitation kinetics of β″ phase
Ialloy + PA	34.8 ± 0.4	$(1.2 \pm 0.1) \times 10^3$	$Y = 1-\exp[-1.5*10^6\ t^2 \exp(-8366/T)]$
IIalloy + PA	40.2 ± 0.8	$(5.0 \pm 0.1) \times 10^3$	$Y = 1-\exp[-2.5*10^7\ t^2 \exp(-9670/T)]$
IIIalloy + PA	42.2 ± 0.7	$(8.6 \pm 0.1) \times 10^3$	$Y = 1-\exp[-7.3*10^7\ t^2 \exp(-10156/T)]$
IValloy + PA	53.2 ± 1.2	$(1.3 \pm 0.1) \times 10^5$	$Y = 1-\exp[-1.6*10^{10}\ t^2\exp(-12{,}800/T)]$
Ialloy + PA + NA	70.2 ± 0.5	$(7.7 \pm 0.1) \times 10^6$	$Y = 1-\exp[-6.0*10^{13}\ t^2 \exp(-16886/T)]$
IIalloy + PA + NA	69.4 ± 0.8	$(6.4 \pm 0.1) \times 10^6$	$Y = 1-\exp[-4.1*10^{13}\ t^2 \exp(-16714/T)]$
IIIalloy + PA + NA	62.4 ± 1.2	$(1.0 \pm 0.1) \times 10^6$	$Y = 1-\exp[-1.0*10^{12}\ t^2 \exp(-15{,}010/T)]$
IValloy + PA + NA	55.0 ± 1.3	$(1.6 \pm 0.1) \times 10^5$	$Y = 1-\exp[-2.5*10^{10}\ t^2 \exp(-13{,}226/T)]$

precipitation, as shown in Table 2. Based on the activation energy and other parameters, the precipitation kinetics of β″ phase formed in the alloys with different quenching rates has been also established in Table 2, which can be better used to predict the precipitation.

3.2. *Precipitation hardening behaviors*

The precipitation hardening behaviors of the alloys with different quenching rates are shown in Fig. 4. It can be seen that the micro-hardness of alloys at the pre-aged state with different quenching rates are similar around 86–89 HV, as shown in Fig. 4(a). The time for alloys reaching the peak aging state are all 3 h, but a slight difference in the micro-hardness value of the peak aged alloys with different quenching rates still can be seen. The micro-hardness increments of the alloy with the quenching rates I, II and III that all quenched in water medium are similar, i.e., distributing in the range of 129.5–132.2 HV, which are lower than that (133.7 HV) of quenching rate IV as shown in Fig. 4(a). Additionally, the hardness of alloys after aged at 185 °C for 20 min with the quenching rates I, II and III are also similar, they were 99.6 HV, 97.6 HV, and 98.2 HV, respectively. However, the alloy with the quenching rate IV has the highest micro-hardness in this state, i.e., 104.5 HV. It can be seen that the highest micro-hardness increment of the alloys after aged at 185 °C for 20 min appears in oil-quenched alloy with the slowest quenching rate, as shown in Fig. 5.

The micro-hardness of pre-aged alloy increases slightly and reaches the stable values after 14-day natural aging. The micro-hardness appears as concave curve in the early stage of artificial aging process for the four alloys, which is corresponding to the re-dissolution of clusters below the critical size that formed during the pre-aging and natural aging 14

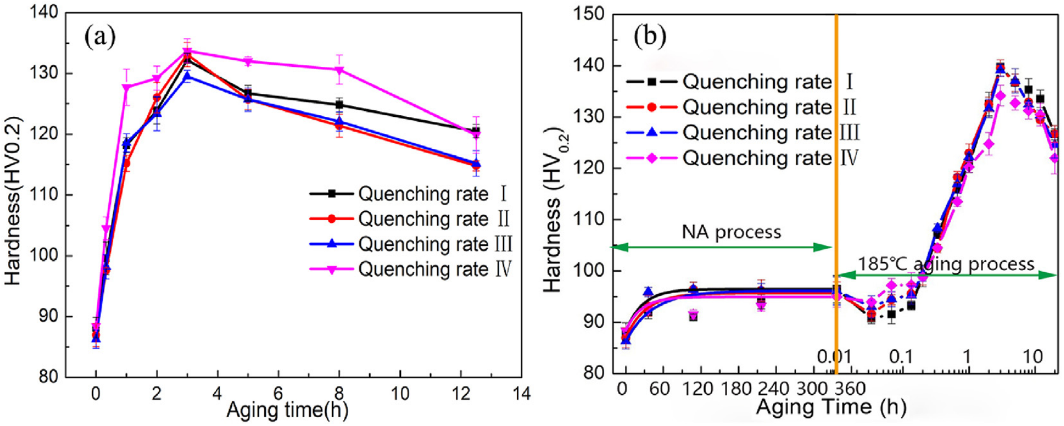

Fig. 4 – **The micro-hardness changes of the pre-aged alloys during the different aging processes (a) 185 °C artificial aging process, (b) the natural aging 14 days +185 °C aging process.**

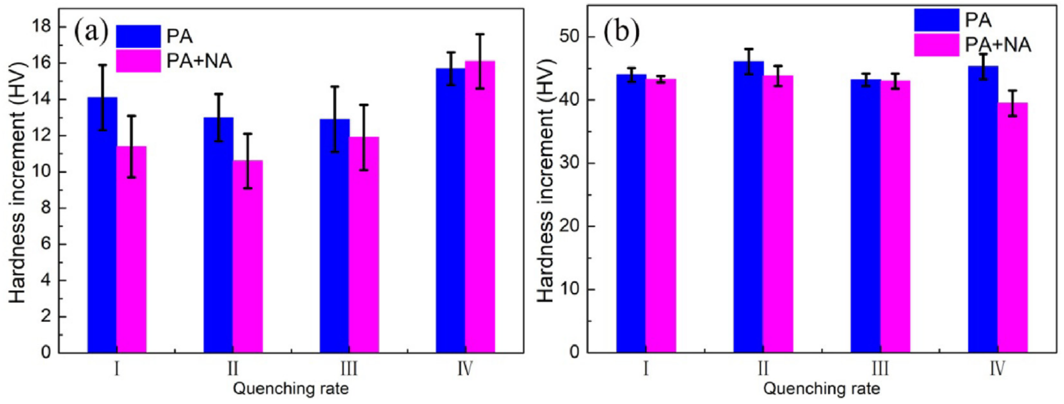

Fig. 5 – **The micro-hardness increment of the pre-aged alloys after aging at 185 °C for 20 min (PB) or 3 h (T6) (a) aging at 185 °C for 20 min, (b) aging at 185 °C for 3 h.**

days. The re-dissolution phenomenon of the alloy with quenching rate I is the most obvious, and it is gradually decreased with reducing the quenching rate, as shown in Fig. 4(b). Additionally, the needed time to reach the peak aging state is basically similar for the T4P treated alloys, i.e., 3 h. The hardness of alloys in the peak aging state with the quenching rates of I, II, III is basically the same, i.e., distributing in the range of 139–140 HV, while the hardness of alloy with quenching rate Ⅳ is reduced to the value of 134.2 HV. For the alloys quenched in water, the micro-hardness increment (11.4 HV, 10.6 HV, and 11.9 HV for quenching rate I, II and III, respectively) after aging at 185 °C for 20 min are much lower than those of the alloys treated without 14-day natural aging. Whereas, the micro-hardness increment (i.e., 16.1 HV), of the alloy with the quenching rate IV can be increased, and much higher than that of the alloy without 14-day natural aging, as shown in Fig. 5. All of these indicate that the age-hardening response of alloys is coupling controlled by both the quenching rate and pre-aging.

3.3. *Mechanical property characterization*

In order to better indicate the synergistic influence of quenching rates and pre-aging on the mechanical properties, the mechanical properties of alloys treated by the different aging processes have been measured as shown in Fig. 6. The yield strength (YS) of alloys in the T4P state and quenched in water is deceased with the reduction of quenching rate, the values for the quenching rate I, II and III are 201.6 MPa, 198.8 MPa, and 177.3 MPa, respectively. However, for the alloy with the quenching rate Ⅳ, its yield strength can still reach 197.7 MPa, which is much higher than that of quenching III. Additionally, the ultimate tensile strength of the four alloys basically keeps the same trend, the value for the quenching rate I, II, III and IV are 346.3 MPa, 341.5 MPa, 325.4 MPa and 339.9 MPa, as shown in Fig. 6 and Table 3.

The mechanical properties of the T4P treated alloys in the paint baking (PB) state (2% pre-strain + 185 °C/20 min) are shown in Table 3. It can be seen that the yield strengths of alloys quenched in water are similar. However, for the alloy quenched in oil, both the yield strength and ultimate tensile strength are higher than those of water quenched alloys (as shown in Table 3). Accordingly, the corresponding bake hardening increment of alloys quenched with different rates are also quite different with each other, and the highest value (i.e., 145.2 MPa), can be found in the alloy with the quenching rate of IV. The bake hardening increment is also much higher than those of traditional Al–Mg–Si–(Cu) alloys (such as, 6016

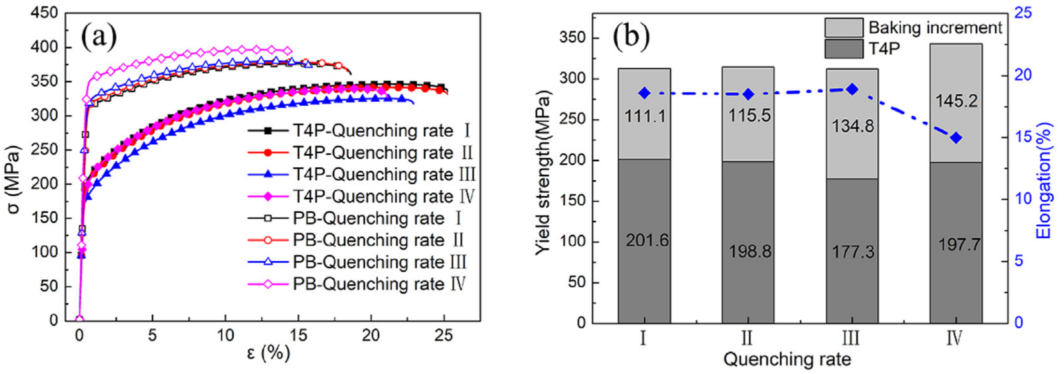

Fig. 6 – **the mechanical properties of alloys in the different aging states, (a) the engineering stress–strain curves in the T4P and PB state, (b) the YS increment and elongation after the PB treatment.**

Table 3 – The mechanical properties of alloys in the T4P and PB states.

Quenching rate	T4P state			PB state			YS increment (MPa)
	YS (MPa)	UTS (MPa)	Elongation (%)	YS (MPa)	UTS (MPa)	Elongation (%)	
I	201.6	346.3	25.0	312.7	376.6	18.6	111.1
II	198.8	341.5	25.1	314.3	378.3	18.5	115.5
III	177.3	325.4	23.6	312.1	380.1	18.9	134.8
IV	197.7	339.9	22.9	342.9	397.1	15.0	145.2

and 6111 alloys) with optimized pre-aging treatments (as shown in Fig. 6 and Table 3) [8,10,42].

3.4. *TEM analysis*

3.4.1. *Paint baking (185 °C/20 min) state*

In order to analyze the synergistic influence of quenching rate and pre-aging on the microstructure of alloys, the detailed TEM observation was carried out as shown in Fig. 7. The distortion of alloys matrix during the quenching process normally leads to the formation of dislocation and vacancies, and the number density and morphology of dislocation and vacancies in Al alloys can be greatly affected by the used quenching rate [43,44]. From Fig. 7, it can be seen that both the second phases with a size of 0.1–0.4 μm and dislocation can be found in the alloy after pre-aging + aging treatment of 185 °C/20 min. As the same composition for treated alloys, the black particles observed in the alloy matrix are determined as the iron-rich phases (as shown in Fig. 7(a)–(e)). These fine iron-rich phases can pin the movement of dislocation formed by the appearance of stress filed after quenching, and the number density of dislocation decreases with the reduction of quenching rate. It can be seen that the lowest number density of dislocation appears in the alloys with quenching rate IV (as shown in Fig. 7).

Besides the dislocation and iron-rich phases, many fine pre-β'' precipitates or GP zones can be observed in the alloys with different quenching rates (as shown in Fig. 7). The different distribution of these precipitates directly results in the different YS increments of alloys after PB treatment. In comparison, it can be seen that with the decrease of quenching rate, the number density of pre-β'' precipitates is also decreased. However, the size of pre-β'' precipitates formed in the oil-quenched alloy is much larger than those of the water quenched alloys (as shown in Fig. 7).

3.4.2. *Peak aging state*

With further aging to peak aging state, the distribution of precipitates in the alloys treated by pre-aging + peak aging at 185 °C also changes greatly as shown in Fig. 8. From it, it can be seen that the size of precipitates has been increased to around 3–5 nm, and their sizes increase with the increase of quenching rate, and the precipitates formed in the oil-quenched alloy have the smallest size. Additionally, the number density of precipitates in the water quenched alloys is basically the same with each other. And it is difficult to see a great difference in the number density of precipitates in the four alloys with different quenching rates (as shown in Fig. 8).

Besides the distribution of formed precipitates, the synergistic influence of quenching rate and pre-aging on the structure, orientation and lattice parameters of precipitates can be also analyzed by HRTEM characterization. Fig. 9 shows the HRTEM microstructure and phase analysis of alloys in the peak aging state (185 °C/3 h). The main precipitates in the peak aging state are β'' phase, which is semi-coherent with Al matrix (as shown in Fig. 9). It has been found that the imbedded β'' phases normally follow the orientational relationship [45], $(010)_{\beta''}//\{001\}_{Al}$, $[001]_{\beta''}//<310>_{Al}$, $[100]_{\beta''}//<230>_{Al}$. For the precipitates formed in the peak aged alloy with quenching rate I, the orientational relationship between β'' precipitates and Al matrix are as follows, $(010)_{\beta''}//(001)_{Al}$, $[001]_{\beta''}//[-310]_{Al}$, $[100]_{\beta''}//[230]_{Al}$, as shown in Fig. 9(a). And the lattice parameters of precipitates are $a = 1.506$ nm, $c = 0.670$ nm, $\beta = 106.4°$, as shown in Table 4. With the decrease of quenching rate, although the morphology of β'' precipitates is basically the same, yet, the orientational relationship between β''

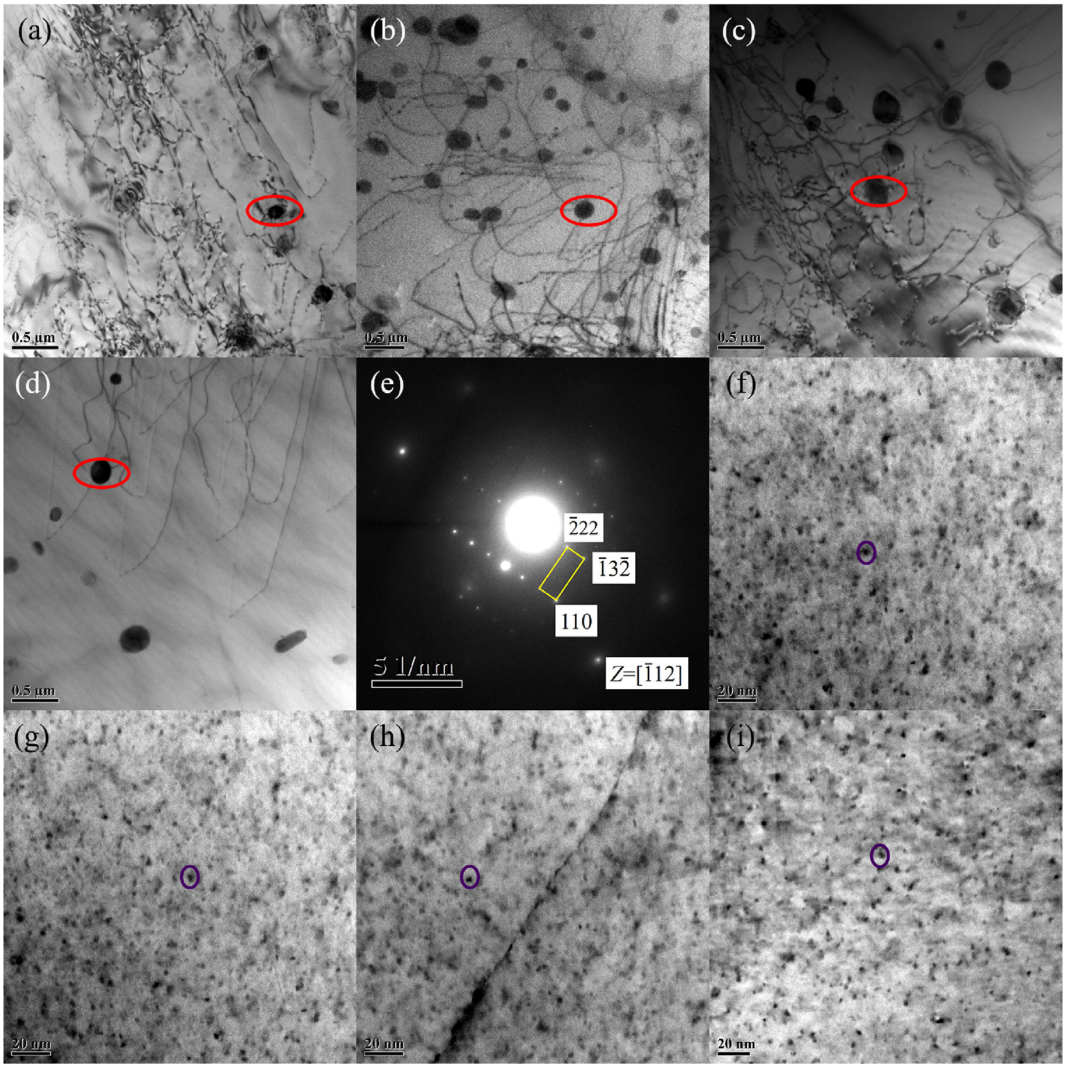

Fig. 7 – The distribution of dislocation and second phases in the alloys after pre-aging + aging treatment of 185 °C/20 min, (a), (f) quenching rate I, (b), (g) quenching rate II, (c), (h) quenching rate III, (d), (e), (i) quenching rate Ⅳ, (e) the diffraction pattern of iron-rich phase (the phase in the red circle).

precipitates and Al matrix have been changed greatly, they are as follows, $(010)_{\beta''}//(001)_{Al}$, $[001]_{\beta''}//[130]_{Al}$, $[100]_{\beta''}//[3-20]_{Al}$ and $(010)_{\beta''}//(001)_{Al}$, $[001]_{\beta''}//[130]_{Al}$, $[100]_{\beta''}//[3-20]_{Al}$ for the quenching rate II and III, respectively, as shown in Fig. 9(b) and (c). And the lattice parameters of the precipitates are changed to the values, $a = 1.505$ nm, $c = 0.670$ nm, $\beta = 106.6°$ and $a = 1.489$ nm, $c = 0.667$ nm, $\beta = 106.3°$, respectively. And for the oil quenched alloy, the orientational relationship between β″ precipitates and Al matrix are as follows, $(010)_{\beta''}//(001)_{Al}$, $[001]_{\beta''}//[1-29,47]_{Al}$, $[100]_{\beta''}//[320]_{Al}$, as shown in Fig. 9(d). The corresponding lattice parameters of the precipitates formed in the oil quenched alloy also change greatly as shown in Table 4. According to the data shown in Table 4, the lattice parameters of Al matrix around the precipitates formed in the alloys slightly decrease compared with the pure Al. And the β angle of the precipitates formed in the alloys with different quenching rates decreases with the quenching rate reducing, and the lowest value appears in the oil quenched alloy. All of these show that both the quenching rates and pre-aging give a synergistic influence on the morphology, size, orientation and distribution of precipitates formed in the peak aged alloys.

4. Discussion

4.1. *Clustering and hardening behaviors in the pre-aging state*

After solution treatment at high temperature, most of precipitates (such as, Mg_2Si, Q phase ($Al_{1.9}Mg_{4.1}Si_{3.3}Cu$) and Si particles) in Al–Mg–Si alloys can be dissolved in alloy matrix, and then a supersaturated solid solution state can be remained after quenching. Thus, besides the solid solution of solutes, a lot of defects (e.g. vacancies and dislocation) can be also formed in quenched alloys. It has been found that with the decrease of quenching rate, the vacancy concentration in

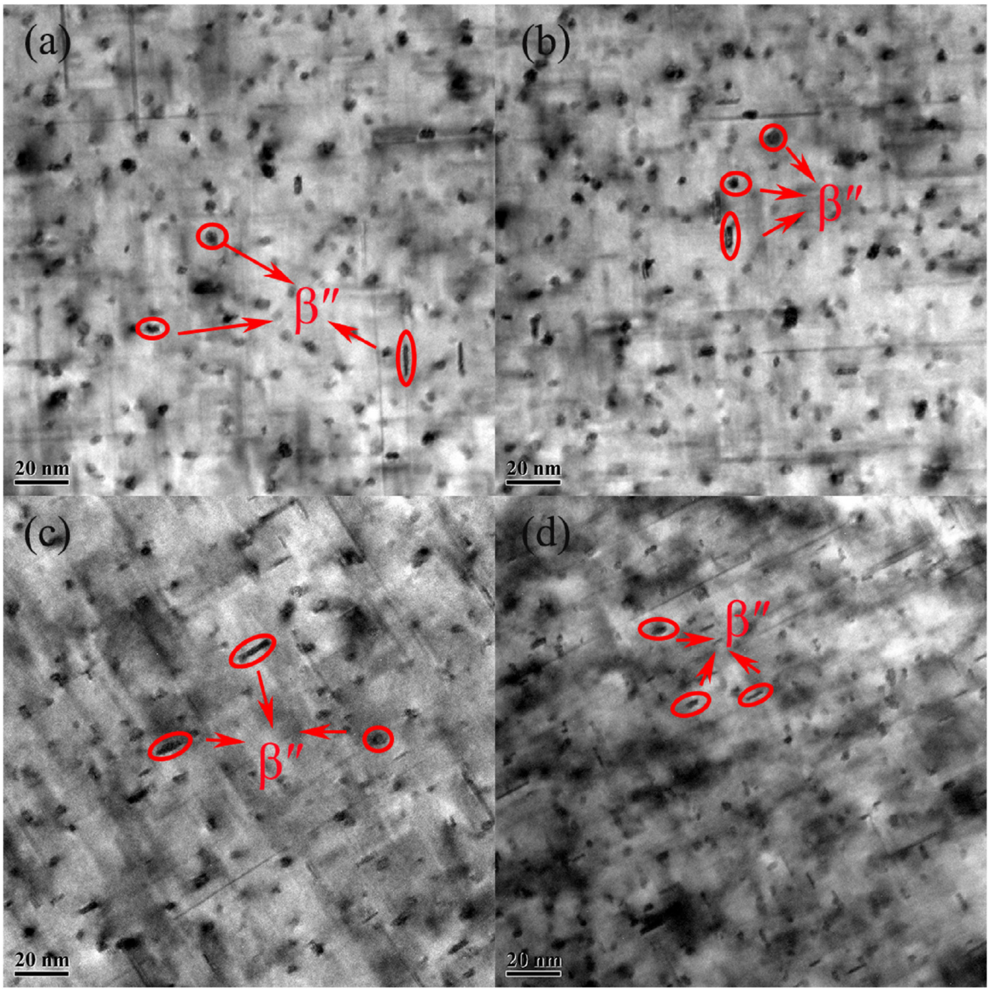

Fig. 8 – The distribution of precipitates formed in the alloys after pre-aging + peak aging treatment of 185 °C/3 h, (a) quenching rate I, (b) quenching rate II, (c) quenching rate III, (d) quenching rate IV.

quenched alloys can be also decreased [48]. If the alloy is quenched with low a quenching rate, the nucleation and growth of precipitates during the pre-aging should be also decreased, which directly results in the low number density of solute clusters in pre-aged alloys with a low quenching rate. Thus, the yield strengths of water quenched alloys in the pre-aging state decrease with quenching rate. However, for the oil quenched alloy, even the quenching rate is the lowest compared with the other three water quenched alloys, both the nucleation and growth rates should be also the lowest in the pre-aging treatment, but the yield strength of alloy in the pre-aging state is not the lowest among them. The reason for this should be resulted from the formation of solute clusters during the oil quenching process. Accordingly, it is greatly important to coupling control of quenching and pre-aging in order to improve the age hardening response of Al–Mg–Si–Cu–Zn series alloys.

4.2. *Age hardening behaviors in the PA + (NA) + AA process*

For pre-aged alloys, if the alloys treated with different quenching rates are directly aged at 185 °C, the formed solute clusters in pre-aging state can further grow and transform into β″ precipitates. And the age hardening and precipitation behaviors at 185 °C are both closely related with the quenching rate. For example, with the decrease of quenching rates used in the water quenched alloys, the bake hardening increments (HV) of alloys also decrease (as shown in Fig. 5). The reasons for this is mainly resulted from the following points, with the decrease of quenching rate, the number density of vacancies formed after quenching should be also decreased. This directly results in the lower nucleation and growth rates. Thus, both the number density and size of solute clusters formed in the low temperature pre-aging should be also much smaller or lower (corresponding to the lower yield strength in the pre-aging state). And then, the number density of dissolved solute clusters during the high temperature should be much higher due to their smaller size and lower stability, which directly results in the lower number density of fine precipitates and lower bake hardening increment (as shown in Figs. 5 and 7). In comparison, if the quenching rate is higher, the vacancy concentration is also increased in the quenched alloys, which directly results in the formation of much more and more stable solute clusters during the pre-aging process. These solute clusters can serve as the nucleation sites of precipitates, and directly grow the corresponding precipitates

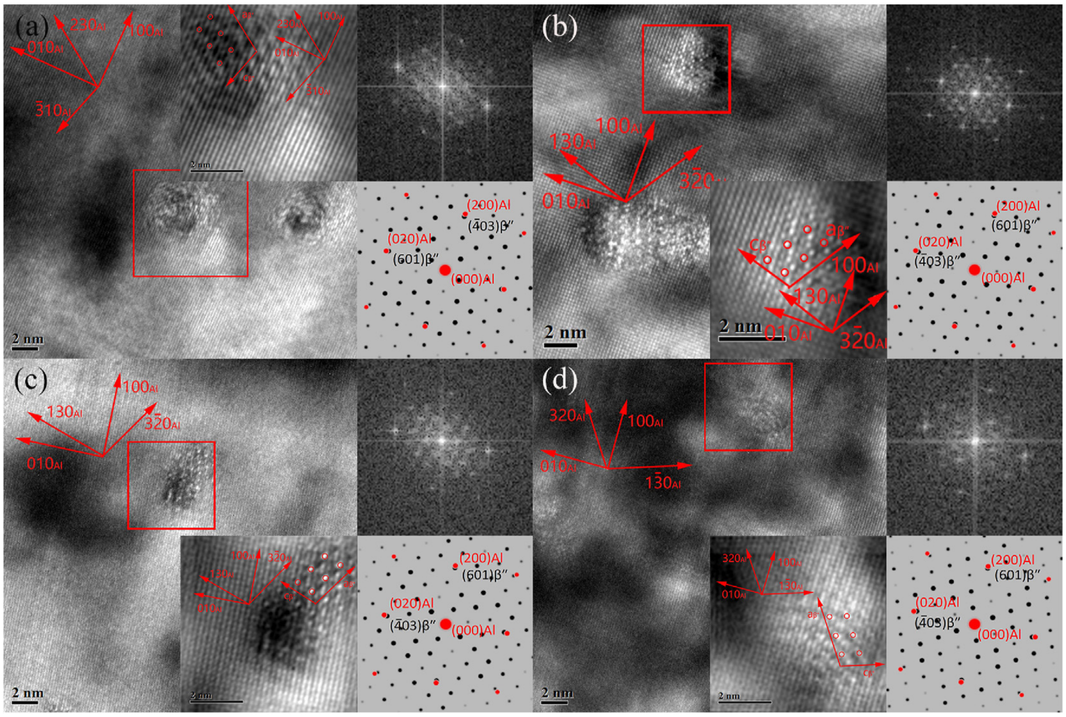

Fig. 9 – The HRTEM characterization of β″ phases formed in the alloys after pre-aging + peak aging treatment of 185 °C/3 h, (a) quenching rate I, (b) quenching rate II, (c) quenching rate III, (d) quenching rate IV.

Table 4 – The lattice parameters of precipitates and Al matrix around the precipitates in peak aging state.

Quenching rate	Parameters of precipitates			Parameters of Al matrix around the precipitates		
	Phase	Measured	Refs. [41,46]	Al matrix	Measured	Pure Al
I	β″	a = 1.506 nm c = 0.670 nm β = 106.4°	a = 1.534 nm c = 0.683 nm β = 105.3°	Lattice parameters of Al matrix around the precipitates	[100] 2.00 Å [010] 1.99 Å	2.02 Å
II	β″	a = 1.505 nm c = 0.670 nm β = 106.6°			[100] 2.01 Å [010] 2.01 Å	2.02 Å
III	β″	a = 1.489 nm c = 0.667 nm β = 106.3°			[100] 2.00 Å [010] 2.02 Å	2.02 Å
IV	β″	a = 1.499 nm c = 0.665 nm β = 105.6°			[100] 2.00 Å [010] 2.01 Å	2.02 Å

during high temperature aging process, which causes the improved bake hardening increment (as shown in Fig. 5(a)). However, for the oil quenched alloy, lots of solute clusters can be formed during the low rate quenching process, and finally the size, composition and distribution of solute clusters formed after coupling control of quenching and pre-aging should be more reasonable, which causes the higher number density of fine precipitates formed after aging at 185 °C for 20 min (as shown in Fig. 7). Thus, not only the hardness of alloy in the pre-aging state is the highest compared with other water quenched alloys, but also the bake hardening increment of oil quenched alloy is also the highest among them (as shown in Fig. 5). In order to better show the clustering affected by the quenching and pre-aging, the corresponding clustering evolution of alloys treated with different quenching rates is shown in Fig. 10. These different distributions of solute clusters formed after pre-aging also directly affect the precipitate distribution and hardness in peak aging state. From Fig. 4(a), a significant difference in peak hardness can be observed, and the alloy treated with the quenching rate III has the lowest peak hardness, while the highest value appears in the alloy treated with quenching rate IV. Additionally, the oil quenched alloy also possesses the highest hardness increment after peak aging treatment even the highest value in the pre-aging state. Accordingly, it can be found that the coupling control of quenching rate and pre-aging is greatly important for the formation of solute clusters and precipitation behavior at high temperature.

Besides the synergistic influence of quenching rate and pre-aging on age hardening response and precipitation behaviors of Al–Mg–Si–Cu–Zn alloys, the 14-day natural aging after the pre-aging treatment also gives a significant effect on the precipitation behaviors of alloy aged at 185 °C. Based on the DSC and

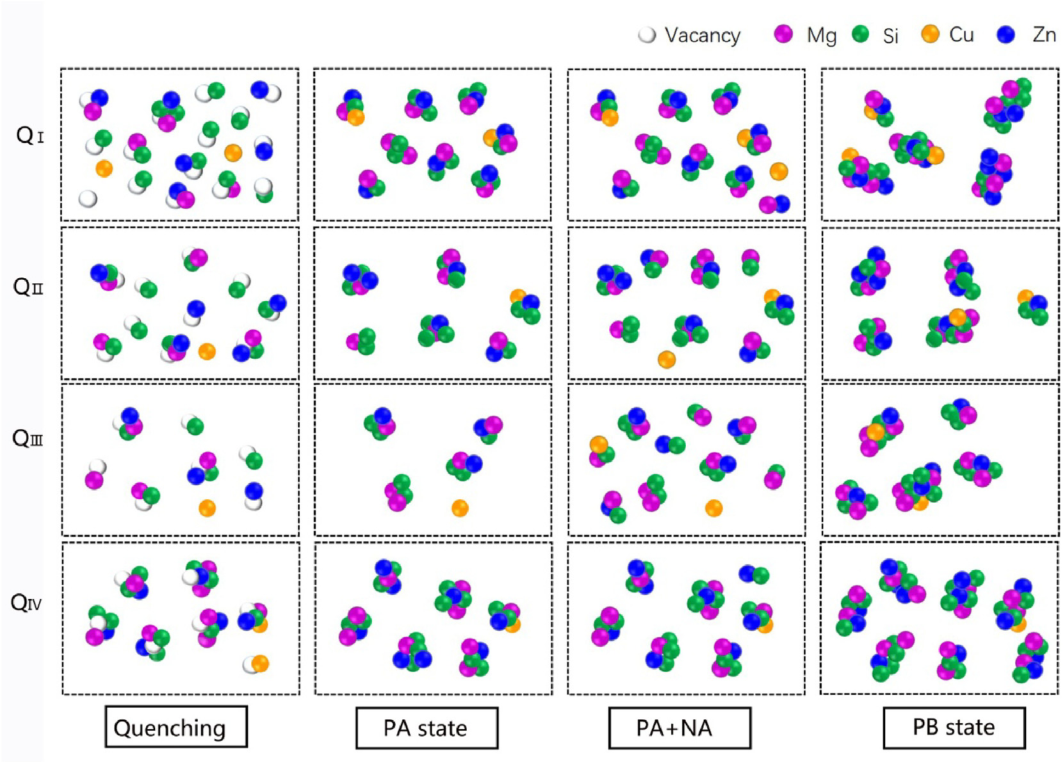

Fig. 10 – The clusters evolution process at different state for different quenching rate alloy.

hardness measurements (as shown in Figs. 2 and 4), it can be seen that the micro-hardness of alloys increases at the initial stage of natural aging, and gradually reaches a stable value (as shown in Fig. 4(b)). And then, if the alloys are aged at 185 °C, the four alloys all exhibit a phenomenon of decrease in hardness, and the decrease level of hardness reduces with the decrease of quenching rate (as shown in Fig. 4). This phenomenon is mainly resulted from the formation of unstable solute clusters during the 14-day natural aging (as shown in Fig. 10). Additionally, the formed unstable solute clusters also affect the formation, dissolution of solute clusters during DSC heating process (as shown in Fig. 2). It has been also found that if Al–Mg–Si alloys in solid state or low temperature pre-aging state, a long time natural aging can give a similar deterioration effect on the bake hardening response [49–53]. The main reasons on the deterioration effect can be summarized as follows, (1) some fine clusters with a low Mg/Si ratio can be formed during natural aging, they cannot serve as the nucleation sites of β″ precipitates; (2) the supersaturated solute atoms can be consumed during natural aging owing to the formation of unstable solute clusters, which reduce the driving force of precipitation during high temperature aging process.

In addition, based on the hardness increments of alloys after aged at 185 °C for 20 min or 3 h (as shown in Fig. 5), it can be also found that although the deterioration effect of natural aging has been greatly reduced after coupling control of quenching rate and pre-aging, yet, they still exhibit a different influence level or trend. The pant baking hardness increments of water quenched alloys treated with the pre-aging + natural aging are all decreased compared with the alloys treated with the pre-aging only, and the increment values of three alloys are basically the same (as shown in Fig. 5), indicating that the influence of quenching rate on the bake hardening response can be reduced by the long time natural aging. However, for the oil quenched alloys, the long time natural aging basically gives a poor effect on the paint baking hardness increment (as shown in Fig. 5), which is mainly results from the formation of stable solute clusters after the coupling control of quenching rate and pre-aging (as shown in Fig. 10). However, with the increase of aging time to 3 h (corresponding to peak aging state), both the peak hardness and hardness increments are changed greatly (as shown in Figs. 4 and 5). Based on the measured tensile properties of alloys treated by pre-aging + natural aging, or pre-aging + natural aging + 2% pre-strain + 185 °C/20 min, the real bake hardening increments (yield strengths) of alloys exhibit a complete different trend (as shown in Fig. 6 and Table 3), especially for the cases of water quenched alloys. However, the highest bake hardening increment (i.e., 145.2 MPa) still appears in the oil quenched alloy. All of these further show that the coupling control of quenching rate and pre-aging really plays a key role in the improvement of bake hardening response of Al–Mg–Si–Cu–Zn–Fe–Mn alloys.

4.3. *Effect of precipitate distribution on the strain hardening behavior*

The formed solute clusters and precipitates by coupling control quenching rate and pre-aging could give a significant effect on the strain hardening behavior of alloys in the different conditions. The strain hardening rate θ can be defined as [54–58],

$$\theta = d\sigma/d\varepsilon \tag{4}$$

where σ and ε are macroscopic true stress and true plastic strain, respectively. Fig. 11 shows strain-hardening rate θ vs. net flow stress ($\sigma - \sigma_{0.2}$) curves. All of the Al alloys in the T4P and PB conditions firstly show a steep hardening decrease with ($\sigma - \sigma_{0.2}$) increase, caused by a short elastoplastic transition [50]. However, with change of quenching rate, the hardening decrease rate also changes greatly. For the T4P treated alloys, the oil quenched alloy with the lowest quenching rate has the highest decrease rate, while the water quenched alloys with three quenching rates basically have the similar decrease rate. However, for the alloys in the PB condition, the alloy treated by water quenching rate III exhibits the highest decrease rate. These differences should be all resulted from the different distributions of solute clusters or precipitates in the alloys with the help of coupling control of quenching rate and pre-aging. And then, with the increase of ($\sigma - \sigma_{0.2}$) value, the strain hardening rate of alloys in the T4P and PB conditions shows an almost linearly decrease with increasing stress, but the alloys in the PB condition exhibit a different trend. The change of strain hardening rate in the different conditions is basically similar to the well-known stage III of strain hardening behavior in fcc polycrystals [55], which is closely related with the distribution of clusters and precipitates. In addition, the intersection of the fitted straight line and the Y axis is considered as θ0 III, denoting the strain hardening rate at the beginning of plastic deformation. For the alloys in T4P condition, the θ0 III values of alloys are slightly increased from 2440.9 MPa (quenching rate I) to 2629.0 MPa (quenching rate IV). However, for the alloy in the PB conditions, the θ0 III value (1274.9 MPa) of alloy treated by the quenching rate IV is the lowest compared with other water quenched alloys (from 1484.5 to 1576.8 MPa). Additionally, the hardening capacity, Hc, of samples can be described by the ratio of ($\sigma_{UTS} - \sigma_{0.2}$) to $\sigma_{0.2}$ [59],

$$Hc = (\sigma_{UTS} - \sigma_{0.2})/\sigma_{0.2} \tag{5}$$

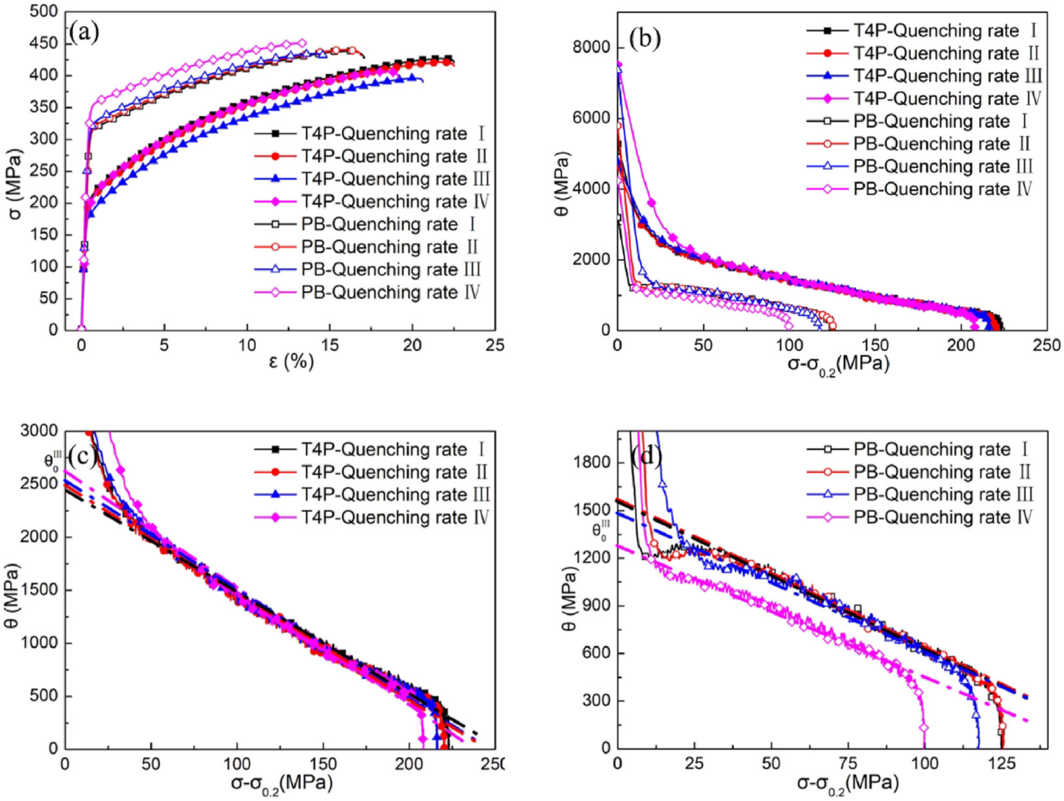

Fig. 11 – Mechanical behaviors of alloys in the different conditions, (a) true stress–strain curves for different quenching rate alloys, (b) θ vs. ($\sigma - \sigma_{0.2}$) for the alloys in (a), (c) strain hardening of alloys at T4P state, partial enlarged view from (b), (d) strain hardening of alloys at PB state, partial enlarged view from (b) (T4P + 2%pre-stretch + 185 °C/20 min).

Table 5 – Mechanical properties of the alloys and other calculated parameters.

Quenching rate	T4P condition			Hc	PB condition			Hc
	YS (MPa)	UTS (MPa)	Elongation (%)		YS (MPa)	UTS (MPa)	Elongation (%)	
I	204.1	428.0	25.0	1.10	313.8	438.5	18.6	0.40
II	200.8	420.8	25.1	1.10	315.0	440.7	18.5	0.40
III	179.8	397.7	23.6	1.21	317.0	434.3	18.9	0.37
IV	198.6	408.1	22.9	1.05	351.5	451.1	15.0	0.28

Based on the definition of Eq. (5), hardening capacity Hc of different samples were calculated and listed in Table 5. It can be found that the value of Hc decreases from 1.21 to 1.05 with decreasing quenching rate from III to IV in the pre-aged samples. The variation of Hc may be closely related to dislocation movements in pre-aged alloys, which is greatly affected by the distribution of solute clusters. However, for the alloys in the PB condition, the Hc values are all greatly decreased (as shown in Table 5). In comparison, the oil quenched alloys still exhibits the lowest value of 0.28. All of these further indicate that the coupling control of quenching rate and pre-aging is greatly important to optimize the distribution of solute clusters and precipitates in the alloys, which further also gives a significantly influence on mechanical properties and strain hardening behaviors in the corresponding condition.

5. Conclusions

(1) The precipitation kinetics of β'' phase formed in the alloys with different quenching rates has been established, the corresponding activation energies of β'' precipitation are greatly dependent on the quenching rate, pre-aging and natural aging together, that is, with the decrease of quenching rate (from quenching rate I to IV), the activation energy of β'' precipitation in the pre-aged alloys increases from 34.8 kJ/mol to 53.2 kJ/mol, while the activation energy of β'' precipitation in the T4P (pre-aging + natural aging 14 days) treated alloys gradually decreases from 70.2 kJ/mol to 55.0 kJ/mol.

(2) With the decrease of quenching rate, the bake hardening increment of alloys gradually increases, and finally based on the coupling control of quenching rate and pre-aging, the oil quenched alloy in the pre-aging + 14-day natural aging condition can exhibit the highest bake hardening increment of 145.2 MPa.

(3) The quenching rate change can result in the significant differences in the size, number density of precipitates in the both paint baking and peak aging states, but the type of precipitates basically keeps the same, i.e., Mg–Si precipitates, and no Mg–Zn precipitates can be observed.

(4) Based on the detailed characterization on microstructure and mechanical properties of alloys treated with different quenching rates, the related mechanisms of coupling control of quenching rate and pre-aging and fast age-hardening response were established in this paper.

Declaration of Competing Interest

The authors declare that they have no known competing financial interests or personal relationships that could have appeared to influence the work reported in this paper.

Acknowledgments

This work was supported by the National Natural Science Foundation of China (No. 51871029, No. 51571023 and No. 51301016), the National Key Research and Development Program of China (No. 2021YFE010225), Government Guided Program-Intergovernmental Bilateral Innovation Cooperation Project (BZ2019019), the Opening Project of State Key Laboratory for Advanced Metals and Materials (2020-ZD02).

REFERENCES

[1] Javidani M, larouche D. Application of cast Al-Si alloys in internal combustion engine components. Int Mater Rev 2014;59:132–58.
[2] Hirsch J, Al-Samman T. Superior light metals by texture engineering: optimized aluminum and magnesium alloys for automotive applications. Acta Mater 2013;61:818–43.
[3] Wang DG, Shu XD, Wang R, Xu S. Mechanism of necking defect of 6082 aluminium alloy rolled by cross-wedge rolling method based on material thermal properties. J Cent South Univ 2020;27:3721–32.
[4] Miller WS, Zhuang L, Bottema J, Wittebrood AJ, De Smet P, Haszler A, et al. Recent development in aluminium alloys for the automotive industry. Mater Sci Eng A 2000;280:37–49.
[5] Hirsch J. Recent development in aluminium for automotive applications. Trans Nonferrous Met Soc China 2014;24:1995–2002.
[6] Ma WP, Wang BY, Xiao WC, Yang XM, Kang Y. Spring back analysis of 6016 aluminum alloy sheet in hot V-shape stamping. J Cent South Univ 2019;26:524–35.
[7] Murayama M, Hono K. Pre-precipitate clusters and precipitation processes in Al-Mg-Si alloys. Acta Mater 1991;47:1537–48.
[8] Guo MX, Zhang YD, Li GJ, Jin SB, Sha G, Zhang JS, et al. Solute clustering in Al-Mg-Si-Cu-(Zn) alloys during aging. J Alloy Compd 2019;774:347–63.
[9] Aruga Y, Kim SN, Kozuka M, Kobayashi E, Sato T. Effects of cluster characteristics on two-step aging behavior in Al-Mg-Si alloys with different Mg/Si ratios and natural aging periods. Mater Sci Eng A 2018;718:371–6.
[10] Guo MX, Sha G, Cao LY, Liu WQ, Zhang JS, Zhuang LZ. Enhanced bake-hardening response of an Al-Mg-Si-Cu alloy with Zn addition. Mater Chem Phys 2015;162:15–9.
[11] Marioara CD, Andersen SJ, Jansen J, Zandbergen HW. The influence of temperature and storage time at RT on nucleation of the β'' phase in a 6082 Al-Mg-Si alloy. Acta Mater 2003;51:789–96.
[12] Zandbergen MW, Cerezo A, Smith GDW. Study of precipitation in Al–Mg–Si Alloys by atom probe tomography II. Influence of Cu additions. Acta Mater 2015;101:149–58.
[13] Weng YY, Jia ZH, Ding LP, Muraishi S, Liu Q. Clustering behavior during natural aging and artificial aging in Al-Mg-Si alloys with different Ag and Cu addition. Mater Sci Eng A 2018;732:273–83.
[14] Yuan B, Guo MX, Wu Y, Zhang JS, Zhuang LZ. Influence of treatment pathways on the precipitation behaviors of Al-Mg-Si-Cu-(Zn)-Mn alloys. J Alloy Compd 2019;797:26–38.
[15] Guo MX, Li GJ, Zhang YD, Sha G, Zhang JS, Zhuang LZ. Influence of Zn on the distribution and composition of heterogeneous solute-rich features in peak aged Al-Mg-Si-Cu alloys. Scr Mater 2019;159:5–8.
[16] Jiao NN, Lai LX, Chen SL, Gao P, Chen JH. Atomic-scale roles of Zn element in age-hardened AlMgSiZn alloys. J Mater Sci Technol 2021;70:105–12.
[17] Francis MF, Curtin WA. Micro alloying for the controllable delay of precipitate formation in metal alloys. Acta Mater 2016;106:117–28.
[18] Werinos M, Antrekowitsch H, Ebner T, Prillhofer R, Uggowitzer PJ, Pogatscher S. Hardening of Al-Mg-Si alloys:

effect of trace elements and prolonged natural aging. Mater Des 2016;107:257–68.
[19] Pazhuhanfar Y, Eghbali B. Processing and characterization of the microstructure and mechanical properties of Al6061-TiB_2 composite. Int J Miner Metall Mater 2021;28:1080–9.
[20] Li GJ, Guo MX, Wang Y, Zheng CH, Zhang JS, Zhuang LZ. Effect of Ni addition on microstructure and mechanical properties of Al–Mg–Si–Cu–Zn alloys with a high Mg/Si ratio. Int J Miner Metall Mater 2019;26:740–51.
[21] Gao GJ, Li Y, Wang ZD, Misra RDK, Li JD, Xu GM. Study of retrogression response in naturally and multi-step aged Al-Mg-Si automotive sheets. J Alloy Compd 2018;753:457–64.
[22] Aruga Y, Kozuka M, Takaki Y, Sato T. Effects of natural aging after pre-aging on clustering and bake-hardening behavior in an Al-Mg-Si alloy. Scr Mater 2016;116:82–6.
[23] Aruga Y, Kozuka M, Takaki Y, Sato T. Evaluation of solute clusters associated with bake-hardening response in isothermal aged Al-Mg-Si alloys using a three-dimensional atom probe. Metall Mate Trans A 2014;45:5906–13.
[24] Birol Y. Pre-aging to improve bake hardening in a twin-roll cast Al-Mg-Si alloy. Mater Sci Eng A 2015;391:175–80.
[25] Falahati A, Lang P, Kozeschnik E. Precipitation in Al-alloy 6016 – the role of excess vacancies. Mater Sci Forum 2012;1:317–22.
[26] Lang P, Falahati A, Ahmadi MR, Warczok P, Povoden-Karadeniz E, Kozeschnik E, et al. Modeling the influence of cooling rate on the precipitate evolution in Al-Mg-Si (Cu) alloys. Mater Sci Technol 2011;1:284–97.
[27] Zhang X, Zhou X, Nilsson J. Corrosion behaviour of AA6082 Al-Mg-Si alloy extrusion: the influence of quench cooling rate. Corros Sci 2019;150:100–9.
[28] Castany P, Diologent F, Rossoll A, Despois JF, Bezençon C, Mortensen A. Influence of quench rate and microstructure on bendability of AA6016 aluminum alloys. Mater Sci Eng A 2013;559:558–65.
[29] Pogatscher S, Antrekowitsch H, Leitner H, Pöschmann D, Zhang ZL, Uggowitzer PJ. Influence of interrupted quenching on artificial aging of Al–Mg–Si alloys. Acta Mater 2012;60:4496–505.
[30] Song FX, Zhang XM, Liu SD, Tian Q, Li DF. The effect of quench rate and over ageing temper on the corrosion behaviour of AA7050. Corros Sci 2015;78:276–86.
[31] Zhang Y, Pelliccia D, Milkereit B, Kirby N, Starink MJ, Rometsch PA. Analysis of age hardening precipitates of Al-Zn-Mg-Cu alloys in a wide range of quenching rates using small angle X-ray scattering. Mater Des 2018;142:259–67.
[32] Kolmogorov AN. On the statistical theory of the crystallization of metals. Bull Acad Sci USSR Math Ser 1937;1:355–9.
[33] Wolverton C. Solute-vacancy binding in aluminum. Acta Mater 2007;55:5867–72.
[34] Liu G, Zhang GJ, Ding XD, Sun J, Chen KH. Modeling the strengthening response to aging process of heat-treatable aluminum alloys containing plate/disc- or rod/needle-shaped precipitates. Mater Sci Eng A 2003;344:113–24.
[35] Du Q, Li YJ. Effect modeling of Cr and Zn on microstructure evolution during homogenization heat treatment of AA3xxx alloys. Trans Nonferrous Met Soc China 2014;24:2145–9.
[36] Guérin M, Alexis J. Identification of the metallurgical parameters explaining the corrosion susceptibility in a 2050 aluminium alloy. Corros Sci 2016;102:291–300.
[37] Gupta AK, Lloyd DJ. Study of precipitation kinetics in a super purity Al-0.8 Pct Mg-0.9 Pct Si alloy using differential scanning calorimetry. Metall Mater Trans A 1999;30:879–89.
[38] Luo A, Lloyd DJ, Gupta AK, Youdelis WV. Precipitation and dissolution kinetics in Al-Li-Cu-Mg alloy 8090. Acta Metall Mater 1993;41:769–76.
[39] Zhang QX, Guo MX, Hu XQ, Zhang JS, Zhuang LZ. Study on kinetics of precipitation in Al-0.6Mg-0.9Si-0.2Cu alloy for automotive application. Acta Metall Sin 2013;49:1604–10.
[40] Kiritani M. Analysis of the clustering process of supersaturated lattice vacancies. J Phys Soc Jpn 1973;35:95–107.
[41] Yang W, Huang L, Zhang R, Wang M, Zhou L, Jia Y, et al. Electron microscopy studies of the age-hardening behaviors in 6005A alloy and microstructural characterizations of precipitates. J Alloy Compd 2012;514:220–33.
[42] Zhu SQ, Shi HC, Yu XY, Yu CY, Ringer SP. Design of solute clustering during thermomechanical processing of AA6016 Al-Mg-Si alloy. Acta Mater 2021;203:116455.
[43] Nicholson RB. Quenching defects in solid solutions and their effect on precipitation. J Phys Radium 1962;23:824–7.
[44] Kiritani M, Weissmann S. Quench-induced defect structure in Al-6.5-at.% Zn. J Appl Phys 1971;42:2603.
[45] Yang WC, Wang MP, Zhang RR, Zhang Q, Sheng XF. The diffraction patterns from β'' precipitates in 12 orientations in Al–Mg–Si alloy. Scr Mater 2010;62:705–8.
[46] Saito T, Wenner S, Osmumdsen E, Marioara CD, Andersen SJ, Røyset J, et al. The effect of Zn on precipitation in Al-Mg-Si alloys. Philos Mag 2014;94:2410–25.
[47] Bryant JD. The Effects of preaging treatments on aging kinetics and mechanical properties in AA6111 aluminum autobody sheet. Metall Mater Trans A 1999;30:1999–2006.
[48] Serizawa A, Hirosawa S, Sato T. Three-Dimensional atom probe characterization of nanoclusters responsible for multistep aging behavior of an Al-Mg-Si alloy. Metall Mater Trans A 2008;39:243–51.
[49] Ding LP, He Y, Wen Z, Zhao PZ, Jia ZH, Liu Q. Optimization of the pre-aging treatment for an AA6022 alloy at various temperatures and holding times. J Alloy Compd 2015;647:238–44.
[50] Cao LF, Rometsch PA. Clustering behaviour in an Al–Mg–Si–Cu alloy during natural ageing and subsequent under-ageing. Mater Sci Eng A 2013;559:257–61.
[51] Engler O, Marioara CD, Aruga Y, Kozuka M, Myhrd OR. Effect of natural ageing or pre-ageing on the evolution of precipitate structure and strength during age hardening of Al-Mg-Si alloy AA 6016. Mater Sci Eng A 2019;759:520–9.
[52] Garric V, Colas K, Donnadieu P, Gilles R, Stéphane U, Bénédicte K. Correlation between quenching rate, mechanical properties and microstructure in thick sections of Al-Mg-Si(-Cu) alloys. Mater Sci Eng A 2019;753:253–61.
[53] Fallah V, Langelier B, Ofori-Opoku N, Raeisinia B, Provatas N, Esmaeili S. Cluster evolution mechanisms during aging in Al–Mg–Si alloys. Acta Mater 2016;103:290–300.
[54] Kocks UF, Mecking H. Physics and phenomenology of strain hardening: the FCC case. Prog Mater Sci 2003;48:171–273.
[55] Zhao CY, Chen XH, Pan FS, Gao SY, Zhao D, Liu XF. Effect of Sn content on strain hardening behavior of as-extruded Mg-Sn alloys. Mater Sci Eng A 2017;24:244–52.
[56] Huang CQ, Deng J, Wang SX, Liu LL. A physical-based constitutive model to describe the strain-hardening and dynamic recovery behaviors of 5754 aluminum alloy. Mater Sci Eng A 2017;699:106–13.
[57] Dorin T, De Geuser F, Lefebvre W, Sigli C, Deschamps A. Strengthening mechanisms of T1 precipitates and their influence on the plasticity of an Al–Cu–Li alloy. Mater Sci Eng 2014;605:119–26.
[58] Zhang P, Shi KK, Bian JJ, Zhang JY, Peng Y, Liu G, et al. Solute cluster evolution during deformation and high strain hardening capability in naturally aged Al-Zn-Mg alloy. Acta Mater 2021;207:116682.
[59] Liu TT, Pan FS, Zhang XY. Effect of Sc addition on the work-hardening behavior of ZK60 magnesium alloy. Mater Des 2013;43:572–7.